Research Square

Preprints are preliminary reports that have not undergone peer review.
They should not be considered conclusive, used to inform clinical practice,
or referenced by the media as validated information.

Assessment of Physiological Cold Exposure Risk in Severe Cold Cities Using a WRF–JOS3 Coupled Framework

Yuliang Xiao
Northeast Forestry University
Xiaokai Chen
Northeast Forestry University
Junliang Cao
cao.junliang@nefu.edu.cn
Northeast Forestry University
Lin Liu
Guangdong University of Technology
Baichao Wu
Northeast Forestry University

Research Article

Keywords: Physiological cold exposure risk, Urban microclimate, WRF, JOS3 model, Safe exposure time, Skin cooling rate, severe cold city

Posted Date: November 18th, 2026

DOI: https://doi.org/10.21203/rs.3.rs-11635956/v1

License: This work is licensed under a Creative Commons Attribution 4.0 International License.
Read Full License

Additional Declarations: No competing interests reported.

Assessment of Physiological Cold Exposure Risk in Severe Cold Cities Using a WRF–JOS3 Coupled Framework

Author name(s): Yuliang Xiao[a,b], Xiaokai Chen[a,b], Junliang Cao[a,b*], Lin Liu[c], Baichao Wu[a]

Affiliation(s):

[a] School of Civil Engineering and Transportation, Northeast Forestry University, 150040, Harbin, China

[b] Institute of Artificial Environment Control and Energy Application, Northeast Forestry University, 150040, Harbin, China

[c] School of Civil and Transportation Engineering, Guangdong University of Technology, Guangzhou, 510006, China

[*]Corresponding author

Corresponding author: Junliang Cao

Corresponding author email address: caojunliang@nefu.edu.cn

Abstract

Cold waves pose substantial health risks in severe cold cities, yet conventional assessments based on meteorological thresholds cannot fully represent dynamic human thermophysiological responses or intra-urban microclimatic variation. This study coupled the Weather Research and Forecasting (WRF) model with the JOS3 human thermoregulation model to develop a human-centric framework linking environmental stress, physiological response, and integrated cold exposure risk. A typical cold-wave event in Harbin, China, was examined at 07:00, 12:00, and 20:00. High-density built-up areas (LCZ 1–3) reduced average wind speed by 71%–74% relative to natural reference areas, while air temperature and wind chill temperature were approximately 1.53 °C and 7.3–7.5 °C higher, respectively. The citywide mean Safe Exposure Time was about 40 min in the early morning and at night, with a local minimum of 33 min, but increased to 67.9 min at noon. The maximum hand skin cooling rate reached 0.576 °C/min, indicating strong acute cold stress. The proposed Cold Exposure Risk Index showed mean values of 71.6, 57.4, and 70.7 at 07:00, 12:00, and 20:00, respectively. Risk increased from the dense urban core toward peripheral farmland and riverside areas. The framework advances cold-risk assessment from environmental exposure toward physiologically interpretable evaluation and supports pedestrian-level wind protection

and human-centric climate-resilient planning in severe cold cities.

Keywords: Physiological cold exposure risk; Urban microclimate; WRF; JOS3 model; Safe exposure time; Skin cooling rate; severe cold city

1 Introduction

The increasing frequency and intensity of extreme weather events have become a major environmental issue affecting urban system safety and public health (Arias et al., 2021). Although global average temperatures are on the rise, extreme cold waves in the mid-to-high latitudes of the Northern Hemisphere continue to show significant regional intensification and pose an ongoing threat to the health of residents in severe cold cities (Nie et al., 2025; PoshtMashhadi et al., 2025). Existing research indicates that exposure to low temperatures significantly increases the risk of cardiovascular and cerebrovascular diseases, respiratory diseases, and all-cause mortality; particularly during cold waves, both emergency department visit rates and mortality rates show a marked upward trend (Bu et al., 2025; Chapman et al., 2025; Zhao et al., 2021). Compared to heat waves, the excess mortality risk associated with cold waves often persists for a longer duration and is particularly pronounced among patients with chronic diseases and those exposed to outdoor environments (Lv et al., 2025; Wang et al., 2024). At the same time, due to the highly heterogeneous nature of urban building structures, ventilation conditions, and surface types, the actual risk of cold exposure to humans during the same cold-wave event often varies significantly across different locations (Georgescu et al., 2024). Therefore, identifying the heterogeneity of cold exposure risks within cities during severe cold spells from the perspective of actual human physiological responses has become a key research direction in urban climate and public health.

Current cold exposure risk assessments are primarily based on environmental meteorological indicators. Indices such as wind chill temperature (WCT) and the Universal Thermal Climate Index (UTCI) provide standardized representations of environmental cold stress by integrating air temperature, wind speed, and radiation conditions, and are widely used in cold wave warnings and regional risk zoning (Di Napoli et al., 2020; Lin et al., 2019). However, such indices remain essentially proxy measures of environmental exposure. Their core limitation lies in the fact that risk assessment relies primarily on fixed meteorological thresholds and fails to account for the human body's dynamic thermoregulatory processes,

making it difficult to reflect the actual physiological tolerance differences under varying microclimatic conditions. Recent studies have indicated that thermal comfort or cold risk assessment methods based solely on meteorological parameters cannot fully characterize the actual heat load on the human body in complex urban environments. Particularly at the block scale, the combined effects of wind fields, radiation, and urban morphology can significantly alter human heat exchange processes (J. Huang et al., 2025; Martilli et al., 2024). In severe cold cities, the wind-shading effect generated by building clusters, thermal compensation in street valleys, and localized wind speed enhancement can all lead to significant differences in the degree of physiological cold stress under the same background meteorological conditions, while traditional environmental indicator systems struggle to effectively identify this micro-scale risk heterogeneity.

To improve the physiological realism of risk assessment, human thermophysiological models have increasingly been introduced into outdoor thermal-environment research (Joshi et al., 2025; Wang et al., 2025). Unlike empirical thermal-comfort indices, multi-node models explicitly solve heat exchange between human tissues and the environment and represent cold-regulation mechanisms such as vasoconstriction and shivering thermogenesis (Takahashi et al., 2021; Vellei et al., 2022; Xu et al., 2023). During its development, JOS3 was validated against human-subject data under steady cold conditions and nine dynamic thermal conditions, producing RMSE values of 0.12–0.38 °C for rectal temperature and 0.58–0.83 °C for mean skin temperature (Assaad et al., 2025; Choudhary & Udayraj, 2023; Takahashi et al., 2021). Subsequent studies further evaluated its ability to predict local and mean skin temperatures under simultaneous changes in air temperature, clothing, and activity intensity (Dharmasastha et al., 2024; Liang et al., 2023; Lin et al., 2025; Zhao et al., 2024).

Meanwhile, the development of mesoscale meteorological models has provided essential technical support for high-resolution urban microclimate simulation. In recent years, the Weather Research and Forecasting (WRF) model, combined with multi-layer urban-canopy parameterizations (ML-UCM/BEP) and Local Climate Zone (LCZ) data, has been widely applied to urban thermal-environment and microclimate studies (Allen-Dumas et al., 2024; Cao et al., 2024; Gál et al., 2025; Kong, Xiao, et al., 2025). These approaches can characterize spatial heterogeneity in near-surface air temperature, wind speed, and radiation

fields caused by differences in urban form (He et al., 2019; Smithson & Adams, 2024). Researchers have also begun coupling regional meteorological models with human heat-balance models to evaluate urban heat exposure and physiological heat stress (X. Huang et al., 2025; Martilli et al., 2024). Nevertheless, existing studies mainly address heat risk, while dynamic physiological responses to cold environments remain insufficiently investigated. This gap is especially evident in severe-cold cities, where few studies have coupled the complete chain of urban microclimate, human thermophysiological response, and cold exposure risk. Three limitations remain: (1) most cold-wave assessments rely primarily on meteorological indicators and lack physiological-response constraints; (2) many thermophysiological studies use idealized environments rather than spatially varying urban microclimates; and (3) the influence of intra-urban form on physiological cold exposure risk has rarely been quantified. Translating high-resolution urban microclimate simulations into physiologically meaningful cold exposure risk therefore remains an important research challenge.

Accordingly, this study applies a coupled framework comprising WRF urban microclimate simulation, JOS3 human thermophysiological response, and CERI composite risk assessment. Using a representative cold-wave event in Harbin, the study evaluates the spatiotemporal differentiation of physiological cold exposure risk and the regulatory role of urban form. Compared with conventional assessments based on a single environmental indicator, this approach emphasizes human tolerance and acute cold stress and provides a physiological perspective on cold exposure risk in severe-cold cities. The objectives are to: (1) characterize the spatial distributions of air temperature, wind speed, and WCT during the cold wave; (2) evaluate safe exposure time and acute cold stress under different urban forms; (3) construct the CERI to reveal spatiotemporal risk patterns; and (4) clarify the pathways through which urban form influences physiological cold exposure risk. The findings can support cold-wave risk management, public-health protection, and climate-adaptive urban planning in severe-cold cities.

2 Methodology and data

A coupled framework was established to connect macro-scale meteorological dynamics, micro-scale human thermophysiological responses, and composite risk quantification. The

121 workflow consisted of three stages. First, WRF was used to simulate high-resolution urban
122 microclimate fields. Second, the meteorological outputs were used to drive JOS3 and obtain
123 human thermophysiological responses. Finally, environmental stress and physiological
124 response were integrated into the Composite Cold Exposure Risk Index (CERI) to reveal
125 spatial risk heterogeneity.

126 2.1 Cold-wave data

127 2.1.1 Study area

128 Harbin was selected as the study area. Located in the central part of the Northeast China
129 Plain (125°42′–130°10′ E, 44°04′–46°40′ N), Harbin is influenced by the East Asian winter
130 monsoon and Siberian cold air, resulting in a prolonged cold season and extreme minimum
131 temperatures below −35 °C. The main urban area extends along both banks of the Songhua
132 River. The central city is relatively compact, whereas the periphery contains open low-rise
133 development, sparsely built areas, and natural land covers, producing marked differences in
134 building shelter, surface roughness, and ventilation conditions.

135 2.1.2 WRF configuration

136 WRF version 4.3 was used for the meteorological simulations. The model employed four
137 two-way nested domains with horizontal resolutions of 27 km, 9 km, 3 km, and 0.5 km. The
138 innermost domain (d04) covered the main urban area of Harbin with 138 × 138 grid cells at a
139 resolution of 500 m, allowing neighborhood-scale microclimatic differences to be represented.
140 The vertical domain comprised 58 layers, with enhanced resolution near the surface to better
141 resolve boundary-layer processes.

142 To accurately capture the influence of the complex urban surface on the microclimate,
143 the Multi-Layer Urban Canopy Model (ML-UCM) was adopted as the urban parameterization
144 scheme. This scheme explicitly accounts for radiation shading within street canyons, multiple
145 reflections, and the impact of building height distribution on the wind field. The planetary
146 boundary layer scheme employs the MYJ (Mellor-Yamada-Janjic) scheme, which performs
147 well in simulating a stable boundary layer and is suitable for strong nocturnal inversions
148 under extremely cold conditions. Other physical parameterization schemes include: the
149 WSM6 microphysical scheme, the RRTMG longwave and shortwave radiation scheme, and
150 the Noah land surface process scheme (Cao et al., 2024). To accurately reflect urban surface

characteristics, the study replaced the WRF default land cover types with Local Climate Zone (LCZ) data. The LCZ data were generated based on Landsat remote sensing imagery and building vector data, dividing the central urban area of Harbin into 18 LCZ types (Kong, Xiao, et al., 2025). Fig. 1 shows the study area, the WRF model nesting domains (d01–d04), and the land cover types of the innermost domain (d04).

Initial and boundary conditions were obtained from ERA5 reanalysis data (https://cds.climate.copernicus.eu/) at a spatial resolution of 0.1° × 0.1° and a temporal resolution of 6 h. ERA5 assimilates extensive ground-based and satellite observations, and its applicability in Northeast China has been widely demonstrated (Kong, Liu, et al., 2025). The WRF simulation covered the complete winter from 1 December 2021 to 28 February 2022. Historical meteorological records indicate that Harbin experienced several cold-wave processes during this winter. Among them, 23–24 December 2021 featured a pronounced cooling process associated with the southward movement of Siberian cold air and represented a typical strong-cold-air event in Harbin. On 24 December, the minimum air temperature was approximately −28 °C and the mean wind speed was approximately 4.5 m/s, producing both extremely low temperatures and pronounced wind-chill conditions. The cold-wave process on 24 December 2021 was therefore selected for the subsequent spatial analysis, model validation, and JOS3 calculations (Wei & Sobrino, 2025).

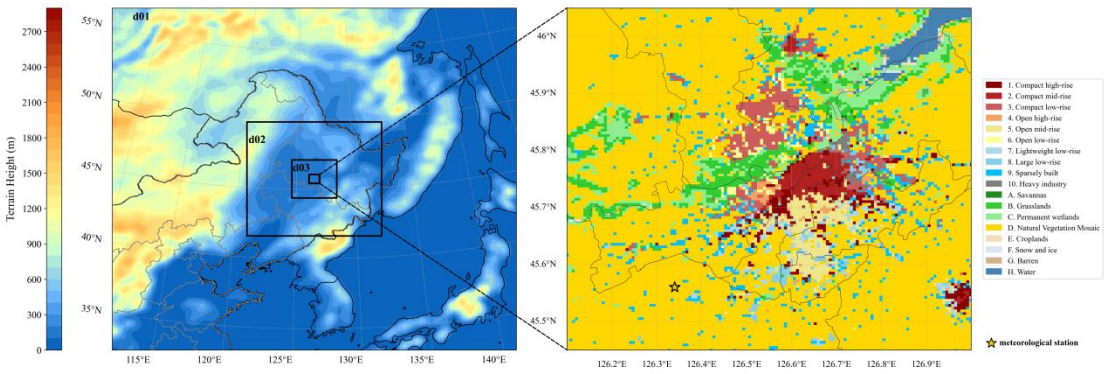


Fig. 1. Nested WRF domains and LCZ classification of the innermost domain (d04).

2.1.3 Meteorological observation data and validation methods

WRF simulations were evaluated against hourly observations from Harbin Taiping International Airport station, obtained from the U.S. National Centers for Environmental Information (NCEI; https://www.ncei.noaa.gov/). Observed variables included air temperature, wind speed, relative humidity, and atmospheric pressure. Root mean square error (RMSE)

was used to quantify the magnitude of simulation–observation differences, and the coefficient of determination (R^2) was used to evaluate consistency in temporal variation (Cao et al., 2023). The research team has accumulated experience in WRF-based urban meteorological simulation for Harbin (Cao et al., 2023; Cao et al., 2024; Kong, Liu, et al., 2025; Kong, Xiao, et al., 2025). Accordingly, simulations for the 23–24 December 2021 cold-wave process were compared hourly with station observations for 2 m air temperature, 10 m wind speed, and relative humidity.

2.2 Simulation of human thermoregulatory responses using the JOS3 model

2.2.1 JOS3 model anthropometric parameters and exposure scenarios

The Joint System Thermoregulation Model (JOS3) was used to calculate human thermophysiological responses. To minimize the impact of individual physiological differences on the results of spatial risk comparisons, standardized population parameters were used as model inputs; specific parameters are shown in Table 1. These settings are primarily intended to characterize the typical physiological state of generally healthy adults engaged in outdoor activities in severely cold urban environments.

Table 1

JOS3 model input parameters for a young male

Parameter	Age	Gender	Height	Weight	Body fat percentage
Value	25 years	Male	1.72 m	68.0 kg	15.0%

Note: Height, weight, and body fat percentage were appropriately adjusted based on the JOS3 model's default parameters and the physical characteristics of the Asian population.

Taking into account the characteristics of urban residents' daily outdoor activities during cold spells, this study conducted simulations at three typical times—07:00, 12:00, and 20:00—representing cold exposure scenarios in the early morning, at noon, and at night, respectively. The activity state was uniformly set to slow walking, with a metabolic rate of 2.0 met, as determined in accordance with the ISO 8996 standard. Clothing conditions consisted of typical everyday winter attire, with localized clothing thermal resistances set for each of the 17 body nodes specified in JOS3, as detailed in Table 2. By standardizing population parameters, activity intensity, and clothing conditions, this study is able to compare the effects

of different urban microclimates on the physiological response to cold exposure while eliminating the interference of individual differences.

Table 2

Thermal resistance distribution of the 17-node JOS3 model

Node	Body part	Clothing thermal resistance (clo)	Node	Body part	Clothing thermal resistance (clo)
1	Head	0.80	10	Right arm	1.80
2	Neck	1.00	11	Right hand	0.90
3	Chest	2.50	12	Left thigh	2.00
4	Back	2.50	13	Left leg	1.60
5	Pelvis	2.00	14	Left foot	1.20
6	Left shoulder	2.00	15	Right thigh	2.00
7	Left arm	1.80	16	Right leg	1.60
8	Left hand	0.90	17	Right foot	1.20
9	Right shoulder	2.00			

Note: The thermal resistance values for each clothing layer reflect the characteristics of typical winter clothing; these values are based on measurements of typical everyday winter clothing in accordance with ISO 9920.

2.2.2 Validation method for the JOS3 model

To evaluate the JOS3 model's ability to simulate changes in human skin temperature under cold exposure conditions, external validation was performed using a publicly available dataset. The validation data were sourced from the dataset titled "Dynamic thermal perception and skin temperature data under whole-body cyclical conditions" published on the Figshare platform (DOI: 10.6084/m9.figshare.21543279). This dataset was derived from dynamic thermal comfort experiments conducted by Vellei et al. (Vellei et al., 2022), involving 64 adult participants who underwent whole-body cyclic cooling and heating processes in a climate-controlled chamber. Each experimental session lasted 180 min, with the first 30 minutes comprising a constant thermal environment phase to bring the subjects close to steady state, followed by a phase of cyclic temperature changes. During the experiment, data

on indoor thermal environment parameters, human skin temperature, and subjective thermal sensations, thermal comfort, and thermal preferences were recorded simultaneously.

From this dataset, cooling exposure segments with complete environmental parameters and continuous skin temperature records were selected as validation samples. During validation, environmental parameters such as air temperature, relative humidity, wind speed, and radiation from the experimental records were used as inputs for the JOS3 model, which was configured based on the individual subject parameters, activity status, and clothing conditions recorded in the dataset. Subsequently, JOS3 was run using a minute-by-minute time-varying forcing approach to simulate skin temperature changes during the corresponding exposure process, which were then compared with the measured skin temperature sequences.

Since the subsequent risk assessment focuses on the rapid cooling process of the hands during cold exposure, hand skin temperature was primarily selected as the comparison variable for model validation. The hand is highly sensitive to changes in the cold environment and can reflect thermoregulatory responses such as peripheral heat dissipation and vasoconstriction during the cooling process. Model performance was evaluated using root mean square error (RMSE), mean absolute error (MAE), and Pearson correlation coefficient (R) to comprehensively assess JOS3's ability to simulate the amplitude, temporal trends, and dynamic response processes of skin temperature changes.

2.2.3 WRF-JOS3 coupling process and calculation of mean radiant temperature

From the validated innermost WRF domain (d04), 2 m air temperature, 10 m wind speed, relative humidity, surface temperature, radiation components, and solar zenith angle were extracted for every grid cell at 07:00, 12:00, and 20:00. These variables were used to drive 120 min JOS3 simulations at a 1 min time step for each grid cell. The 10 m wind speed was retained because it is both a standard near-surface WRF output and the reference-height wind speed specified in the WCT formulation (Lin et al., 2019). Moreover, the ML-UCM and LCZ parameterizations represent first-order urban-form effects on wind attenuation through surface roughness and urban-canopy momentum exchange (Kong, Liu, et al., 2025; Kong, Xiao, et al., 2025). Using the same wind field in WCT and JOS3 ensures input consistency between environmental stress and physiological response and is appropriate for citywide grid-scale comparisons; conversion to pedestrian-height wind speed can be addressed in future

street-scale refinements.

The mean radiant temperature （T_{mrt}） is a key parameter for radiative heat transfer between the human body and the environment. This study uses the following formula for calculation (Kacker et al., 2024):

$$T_{mrt} = \sqrt[4]{\frac{1}{\sigma}\left[f_a L_{surf}^{\downarrow} + f_a L_{surf}^{\uparrow} + \frac{\alpha_{ir}}{\varepsilon_p}\left(f_a S_{surf}^{dif\downarrow} + f_a S_{surf}^{\uparrow} + f_p I^{*} \right) \right]} \tag{1}$$

Where σ is the Stefan–Boltzmann constant (5.67×10^{-8} $Wm^{-2}\cdot K^{-4}$); f_a is the angular coefficient between the human body and the surrounding surface, for a standing person on open ground, it is taken as 0.5; $L_{surf}^{\downarrow}$ is downward long-wave radiation from the sky (WRF output); $L_{surf}^{\uparrow}$ is upward long-wave radiation from the ground, calculated based on surface temperature:

$$L_{surf}^{\uparrow} = 0.95\sigma T_s^4 + 0.05 L_{surf}^{\downarrow} \tag{2}$$

Where T_s is the surface temperature (WRF output); ε_p is the long-wave emissivity of the human body, taken as 0.97; α_{ir} is the solar radiation absorption coefficient of the human body surface, taken as 0.7; $S_{surf}^{dif\downarrow}$is isotropic shortwave radiation scattering (WRF output); $S_{surf}^{\uparrow}$is surface-reflected shortwave radiation, equal to the difference between downward shortwave radiation and net surface shortwave radiation (both can be calculated from WRF output); $f_p$is the human body projection factor, representing the proportion of the human body surface exposed to direct solar radiation, calculated as follows (Di Napoli et al., 2020):

$$f_p = 0.308\cos\left[\gamma\left(0.998 - \frac{\gamma^2}{50000} \right) \right] \tag{3}$$

Where γ is the solar elevation angle (in degrees), calculated from the solar zenith angle output by WRF; I^{*} is the direct solar radiation intensity, obtained as the ratio of direct solar radiation $S_{surf}^{dif\downarrow}$ to the cosine of the solar zenith angle $cos\,\theta$(Di Napoli et al., 2020):

$$I^{*} = \frac{S_{surf}^{dif\downarrow}}{\cos\theta} \tag{4}$$

Using the above equations, T_{mrt} was calculated for each grid point at the three selected time points. The calculated T_{mrt} values, along with air temperature, wind speed, and relative

humidity, are used as the instantaneous environmental input parameters for the JOS3 model. The initial conditions for the JOS3 simulation were set as follows: core body temperature of 37.0 °C, mean skin temperature of 34.0 °C, and all body segments in a thermoneutral state. The simulation output parameters include minute-by-minute data such as core temperature, skin temperature for each body segment, mean skin temperature, and shivering heat production. The simulation results were used to develop a cold exposure risk index.

2.3 Construction of the Cold Exposure Risk Index (CERI)

To characterize urban cold exposure risk, CERI integrates the Environmental Stress Index (ESI) and Physiological Response Index (PRI). Although both are influenced by external meteorological conditions, they describe different levels of the causal chain: ESI represents the external cold hazard generated by air temperature and wind speed, whereas PRI represents the time-dependent response produced after environmental forcing is modified by human heat balance, clothing, activity, and thermoregulation. Environmental-health and composite-indicator studies commonly integrate external exposure and human response because similar environmental intensity does not necessarily produce identical response rates or tolerance times (Becker et al., 2017; Greco et al., 2019; Schmidt et al., 2015). CERI therefore links environmental stress with physiological response rather than simply assigning repeated weights to the same meteorological information.

2.3.1 Environmental Stress Index (ESI)

The Environmental Stress Index (ESI_i) reflects the objective intensity of cold stress at grid point i at a specific time. It is independent of human models and determined solely by meteorological conditions. Wind chill temperature (WCT) is used as the core indicator, which comprehensively considers the combined effects of air temperature and wind speed. The calculation of WCT varies depending on wind speed (Lin et al., 2019). When $V \geq 1.389 m/s$, the WCT is calculated as follows:

$$WCT = 13.12 + 0.6215 \cdot T_a - 13.9563 \cdot V^{0.16} + 0.4867 \cdot T_a \cdot V^{0.16} \quad (5)$$

When $V < 1.389 \mathrm{m/s}$, the WCT is calculated as follows:

$$WCT = T_a - 1.1448 \cdot V + 0.0968 \cdot T_a \cdot V \quad (6)$$

Here, T_a represents the air temperature at 2 m (°C), and V represents the wind speed at 10 m

(m/s). A lower *WCT* value indicates stronger cold stress. To ensure consistency with the units of other sub-indices, the *WCT* is normalized as follows:

$$ESI_i = \frac{WCT_{max} - WCT_i}{WCT_{max} - WCT_{min}} \times 100 \quad (7)$$

In the equation, WCT_i represents the *WCT* value at grid point i, while WCT_{max} and WCT_{min} represent the maximum and minimum *WCT* values, respectively, across all grid points in the study area over the entire time period. The ESI_i ranges from 0 to 100, with higher values indicating stronger environmental cold stress.

2.3.2 Physiological Response Index (PRI)

The Physiological Response Index (PRI_i) consists of SET and the maximum hand skin cooling rate simulated by JOS3. SET represents the accumulated exposure time required for peripheral temperature to reach a physiologically meaningful threshold, whereas the cooling rate represents the intensity of rapid heat loss during the initial stage of exposure. Cold stress has both duration- and rate-dependent characteristics, and prolonged exposure and rapid peripheral cooling can both affect local functional outcomes (Chapman et al., 2025; Orysiak et al., 2024). Combining these variables avoids evaluating physiological risk solely through either exposure duration or instantaneous cooling intensity.

Safe Exposure Time (SET) was defined as the time from the onset of outdoor exposure until JOS3 first predicted that hand or foot skin temperature reached 25 °C. In this study, 25 °C was treated as an operational threshold for marked peripheral cooling rather than a frostbite threshold. Peripheral skin temperature is closely associated with local cold sensation, tactile function, and manual performance (Chapman et al., 2025; Lehmuskallio et al., 2002; Orysiak et al., 2024), and recent occupational cold-exposure experiments reported skin-temperature thresholds of approximately 25–27 °C when finger and hand dexterity began to decline after rewarming (Chapman et al., 2025). SET therefore represents the physiological and functional tolerance margin before pronounced local cooling occurs. A shorter SET indicates more rapid attainment of the response threshold and higher relative cold exposure risk under standardized conditions.

The hand skin cooling rate (dT_{sk}/dt) is defined as the maximum rate of decrease in hand skin temperature (°C/min) during exposure, reflecting the severity of heat loss from the body.

A faster decline rate indicates more rapid heat loss and more severe cold stress.

The formula for calculating the physiological response index is as follows:

$$PRI_i = w_{SET}\left(1-\frac{SET_i}{SET_{max}}\right)\times 100 + w_{cool}\frac{dT_{sk}/dt|_{max,i}}{(dT_{sk}/dt)_{max}}\times 100 \quad (8)$$

In the equation: SET_i is the SET value at grid point i at a specific time; SET_{max} is the maximum SET value across all grids and time points; $dT_{sk}/dt|_{max,\ i}$ is the maximum hand skin cooling rate at grid point i; $(dT_{sk}/dt)_{max}$ is the global maximum cooling rate; w_{SET} and w_{cool} are weighting coefficients, set to 0.7 and 0.3, respectively, to highlight the dominant role of SET in the physiological response.PRI_i ranges from 0 to 100, with higher values indicating a higher physiological risk.

2.3.3 Calculation of the Cold Exposure Risk Index

Based on the Environmental Stress Index (ESI) and the Physiological Response Index (PRI), a comprehensive Cold Exposure Risk Index (CERI) is constructed through weighted summation:

$$CERI_i = w_E \cdot ESI_i + w_P \cdot PRI_i \quad (9)$$

Here, w_E and w_p represent the weights for environmental stress and physiological response, respectively, such that $w_E+w_p=1$.

The Analytic Hierarchy Process (AHP) (Saaty, 1980) was used to determine the weights of environmental stress and physiological response. AHP converts an explicit theoretical hierarchy and judgments of relative indicator importance into quantitative weights and has been widely used in health and environmental composite-index research (Greco et al., 2019; Schmidt et al., 2015). Because CERI is intended to extend assessment from the external cold environment toward physiological response, physiological response was assigned a value of 2 relative to environmental stress in the pairwise comparison matrix, corresponding to ‘slightly more important.’ This produced weights of 0.40 for environmental stress and 0.60 for physiological response. The consistency ratio was CR = 0.00, below the conventional AHP threshold of 0.10, indicating internal consistency of the judgment matrix.

The CERI ranges from 0 to 100, with higher values indicating a higher risk of cold exposure. Based on the CERI value, risk is classified into five levels: low risk (0–20), lower

risk (20–40), moderate risk (40–60), higher risk (60–80), and high risk (80–100). The corresponding CERI values can be calculated for different time points to reveal the spatiotemporal variation in cold exposure risk.

3 Results and discussion

3.1 Validation of the JOS3 human thermophysiological model

Before conducting city-scale cold exposure simulations, the performance of JOS3 under cold exposure was evaluated. Minute-by-minute air temperature, mean radiant temperature, relative humidity, and wind speed from the public experimental dataset were used to drive JOS3, and the simulated hand skin temperature was compared point by point with the measured series.

Fig. 2 shows the measured and simulated hand skin temperatures during the 180 min dynamic exposure. JOS3 reproduced the overall cooling trajectory, with an RMSE of 1.108 °C, an MAE of 0.869 °C, and a Pearson correlation coefficient of R = 0.866. According to commonly used interpretations, R values of 0.70–0.89 indicate a strong linear relationship (Schober et al., 2018), showing that JOS3 captured both the direction and temporal structure of hand skin cooling. Together with the original JOS3 validation under steady cold and dynamic conditions and subsequent studies of local skin temperature (Assaad et al., 2025; Takahashi et al., 2021), these results support its use for relative comparisons of physiological response to cold exposure.

Small deviations and a slight response lag remained during periods of rapid temperature change, but the error magnitude was comparable to that reported in studies predicting local skin temperature with multi-node thermoregulation models (Assaad et al., 2025; Lin et al., 2025; Takahashi et al., 2021). Local skin temperature is sensitive to individual vasomotor regulation, clothing fit, and local convective heat transfer, making some discrepancy physiologically and experimentally reasonable. More importantly, JOS3 reproduced the overall decrease and temporal evolution of hand skin temperature, which are the key characteristics required for comparing SET and maximum cooling-rate differences under standardized human, clothing, and activity conditions.

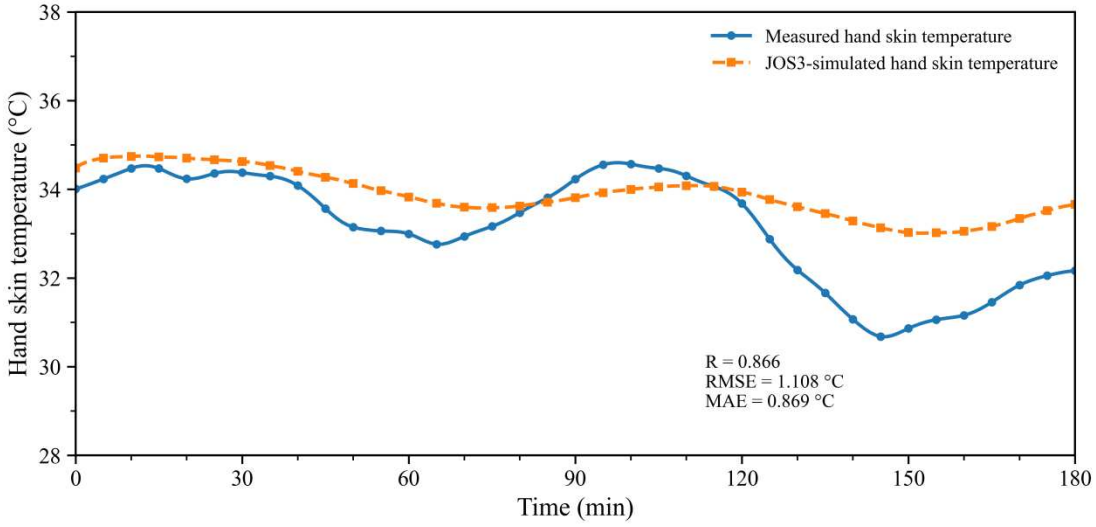


Fig. 2. Comparison between measured and JOS3-simulated hand skin temperature during the 180 min exposure experiment.

3.2 Results and validation of urban microclimate simulations

3.2.1 Validation of WRF simulation accuracy

The validation results indicate that WRF reproduced the temporal variations of near-surface meteorological variables during the cold-wave event (Fig. 3). For 2 m air temperature, R^2 = 0.83 and RMSE = 1.24 °C. For 10 m wind speed, R^2 = 0.65; given the positive relationship between simulations and observations, this corresponds to R = 0.81, which is considered a strong linear correlation (Schober et al., 2018). The wind-speed RMSE was 1.51 m/s, below the 2 m/s reference value commonly used in meteorological-model evaluation (Hanna & Yang, 2001). Relative humidity yielded an RMSE of 8.74% and R^2 = 0.54 and reproduced the dry conditions and temporal variation during the event. Taken together, the correlation and error magnitudes indicate that WRF provided adequate accuracy for subsequent city-scale comparisons of relative microclimatic differences during this cold-wave event.

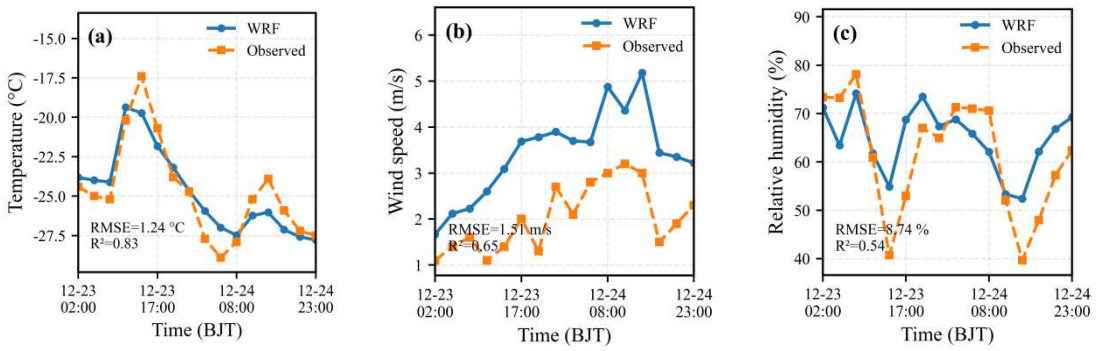


Fig. 3. Comparison between WRF simulations and station observations during the cold-wave event: (a) 2 m air temperature, (b) 10 m wind speed, and (c) relative humidity.

3.2.2 Spatial characteristics of urban meteorology and wind chill index

To examine the role of urban form during the selected cold-wave event, the study area was divided into high-density built-up areas (LCZ 1–3), medium- and low-density built-up areas (LCZ 4–6), and a natural reference area (LCZ D). Fig. 4 presents the spatial distributions of 2 m air temperature (Fig. 4a1–a3), 10 m wind speed (Fig. 4b1–b3), and WCT (Fig. 4c1–c3) at 07:00, 12:00, and 20:00. The following comparisons describe morphological differences under the selected event and model scenario.

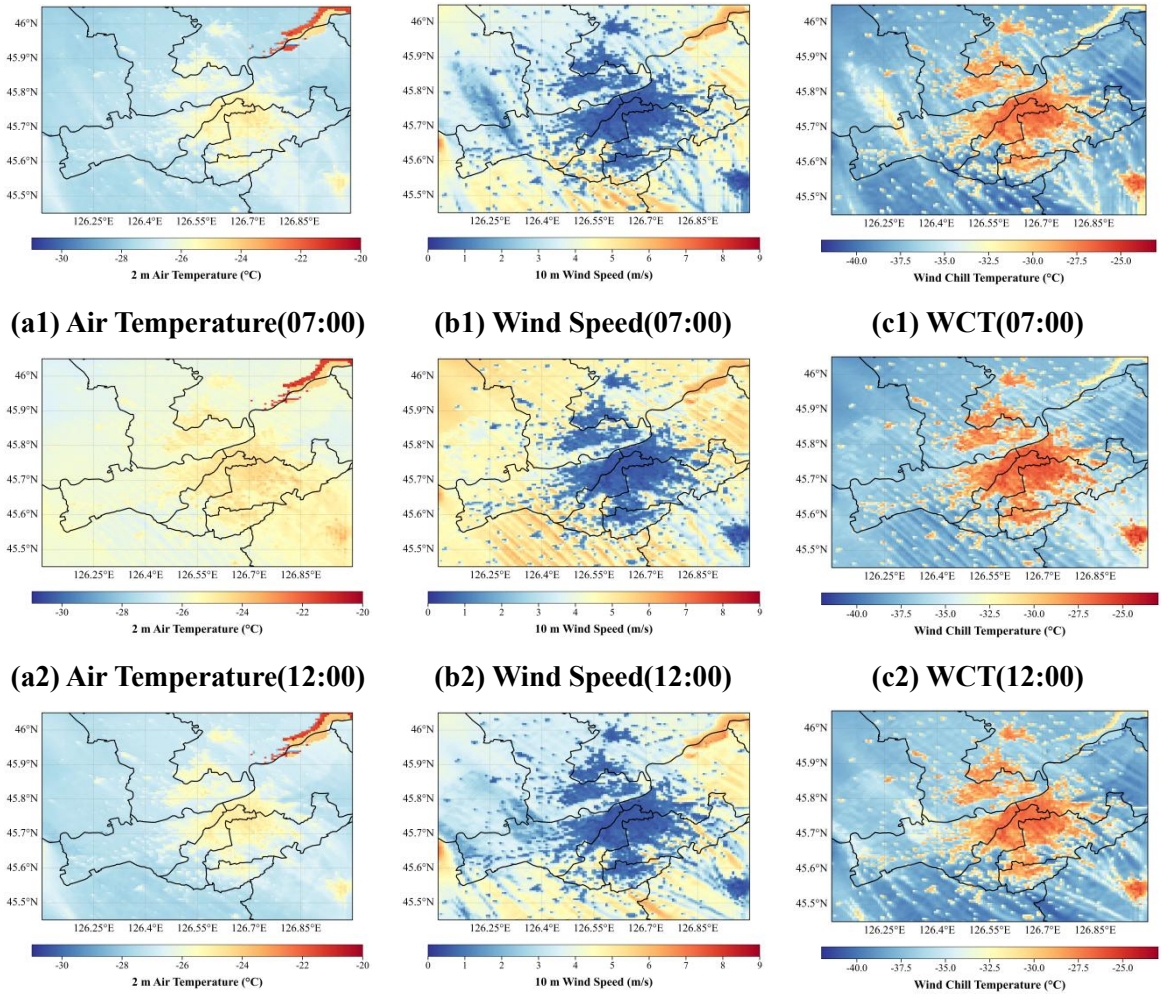
Table 3 summarizes the mean values and domain-wide statistics of air temperature, wind speed, and WCT for each LCZ at the three selected times. Harbin exhibited pronounced intra-urban microclimatic heterogeneity during the event, with building density and spatial openness serving as important controls on the local wind-chill environment. The natural reference area showed relatively high wind speeds of 3.73–4.53 m/s, and the local maximum reached 8.25 m/s at 20:00. By contrast, mean wind speed in high-density built-up areas was only 0.57–0.93 m/s, more than 70% lower than in the natural reference area, demonstrating the damping effect of compact building clusters on the near-surface wind field.

Air temperature showed a modest urban thermal-buffering pattern. At 07:00, the mean air temperature in the high-density built-up area was −25.51 °C, approximately 1.53 °C higher than in the natural reference area, indicating a degree of heat storage and radiative compensation in the built environment during the cold wave. At 12:00, increased shortwave solar radiation raised air temperature across the domain; however, boundary-layer development also increased wind speed, partly offsetting the improvement in the cold environment.

The WCT results further reveal the comprehensive regulatory role of urban form on the actual thermal environment experienced by humans. Due to both higher air temperatures and lower wind speeds, the WCT in high-density built-up areas was more than 7 °C higher than in natural areas, demonstrating a significant wind chill buffering effect; in medium- and low-density built-up areas, the WCT dropped to −35.93 °C at 20:00 under the combined influence of low temperatures and residual wind speeds, with local minimum values reaching −40.91 °C, forming a distinct zone of high wind-chill sensitivity at night.

During the selected event, high-density built-up areas reduced local wind-chill intensity through the combined effects of thermal buffering and wind-speed damping. Compared with the approximately 1–2 °C air-temperature difference, wind speed was reduced by more than 70%, increasing WCT by more than 7 °C relative to the natural reference area. This demonstrates that pedestrian-level wind differences were an important contributor to the spatial differentiation of cold exposure in this case. Physically, dense building clusters increase aerodynamic roughness and reduce the downward transfer of wind momentum to pedestrian height, thereby weakening convective heat exchange between the body and the environment.

These results demonstrate a clear pedestrian-level wind-chill sheltering effect of high-density built environments during the selected cold-wave event, but they do not imply that increasing building density is advantageous under all weather conditions or throughout the year. Wind shelter and heat storage can reduce winter cold exposure, whereas the same form may impede ventilation and retain heat during summer. Conversely, open spaces and ventilation corridors may intensify winter wind chill but improve heat dissipation in warm seasons. Urban-form health effects are therefore event- and season-dependent, and climate-responsive planning should balance winter wind protection with summer ventilation and heat dissipation .



(a1) Air Temperature(07:00) **(b1) Wind Speed(07:00)** **(c1) WCT(07:00)**

(a2) Air Temperature(12:00) **(b2) Wind Speed(12:00)** **(c2) WCT(12:00)**

(a3) Air Temperature(20:00) **(b3) Wind Speed(20:00)** **(c3) WCT(20:00)**

457 Fig. 4. Spatial distributions of 2 m air temperature, 10 m wind speed, and WCT at 07:00,
458 12:00, and 20:00.

459 **Table 3**

460 Average values and global statistics of 2 m air temperature, 10 m wind speed, and WCT for
461 each LCZ at 07:00, 12:00, and 20:00

	Temperature (°C)			Wind Speed (m/s)			WCT (°C)		
	07:00	**12:00**	**20:00**	**07:00**	**12:00**	**20:00**	**07:00**	**12:00**	**20:00**
LCZ1	-25.81	-24.94	-25.77	0.83	0.85	0.84	-28.83	-27.93	-28.82
LCZ2	-25.21	-24.68	-25.11	0.57	0.59	0.58	-27.23	-26.76	-27.17
LCZ3	-26.01	-25.05	-25.77	0.84	0.93	0.83	-29.08	-28.36	-28.80
LCZ4	-25.9	-25.10	-25.80	0.87	0.90	0.86	-29.07	-28.30	-28.94
LCZ5	-25.76	-24.99	-25.80	0.85	0.86	0.83	-28.83	-28.02	-28.81

LCZ6	-26.25	-25.22	-26.00	0.96	1.07	0.95	-29.80	-29.04	-29.48
LCZ7	-25.57	-24.57	-25.61	1.17	1.21	1.16	-29.75	-28.76	-29.79
LCZ8	-26.39	-25.25	-26.37	1.25	1.30	1.18	-30.81	-29.73	-30.61
LCZ9	-26.63	-25.35	-26.51	1.21	1.37	1.20	-31.08	-30.18	-30.92
LCZD	-27.20	-25.89	-27.06	3.82	4.53	3.73	-37.33	-36.7	-37.05
Max	-20.98	-20.42	-20.58	8.24	7.85	8.25	-25.02	-23.98	-25.28
Min	-30.51	-27.12	-29.19	0.01	0.06	0.01	-41.48	-39.75	-40.91
Avg	-27.00	-25.75	-26.87	3.33	3.94	3.26	-36.00	-35.34	-35.75

3.3 Grid-driven human thermophysiological responses

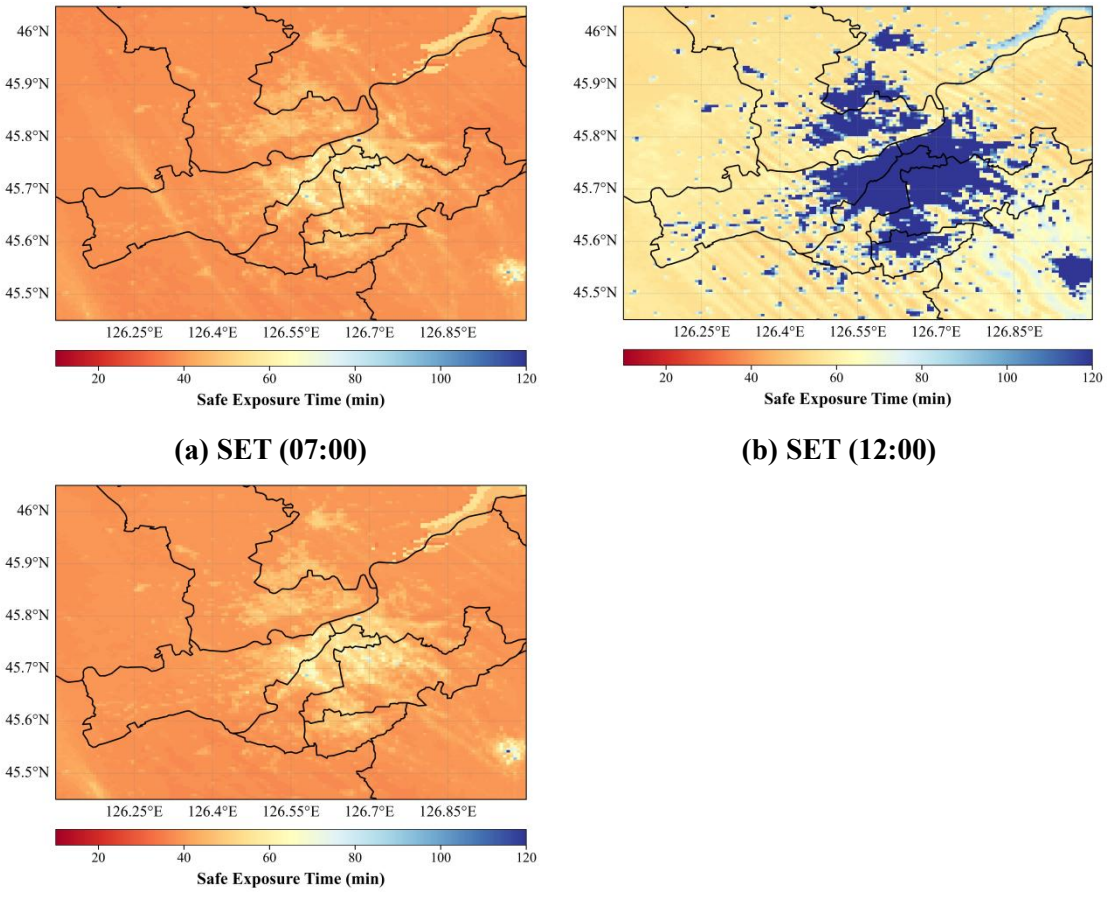
3.3.1 Spatiotemporal variations in safe exposure time (SET)

Based on grid-level microclimate data from the WRF model, the JOS3 model was used to simulate human thermophysiological responses, with the Safe Exposure Time (SET) used to characterize the time required for human hand skin temperature to reach a specified threshold under given conditions. Fig. 5 shows the spatial distribution of SET across the entire city at 07:00, 12:00, and 20:00. The citywide average SET at 07:00 and 20:00 was 40.1 min and 40.6 min, respectively (Table 4), with a local minimum of only 33.0 min (occurring in the LCZ D natural reference area); at 12:00, the citywide average SET increased to 67.9 min, with some grid cells in the central urban area reaching the simulation upper limit of 120 min. These results indicate that, among the three selected time points, cold tolerance duration was shorter at 07:00 and 20:00, while at 12:00, conditions were relatively more favorable due to solar radiation input. High-density built-up areas exhibited relatively longer SET at all three time points during this event; however, this result is subject to the combined constraints of weather conditions, human physiological parameters, clothing, and activity scenarios.

From the perspective of human thermal balance, spatial variations in SET reflect differences in the body's ability to maintain peripheral skin temperature under varying microclimatic conditions. In the early morning and at night, when solar radiation is weak, the body is primarily in a state of continuous net heat loss. Higher wind speeds in open areas further enhance convective heat loss, causing peripheral areas such as the hands and feet to

reach the cold discomfort threshold more quickly, resulting in a significant shortening of SET. Conversely, in high-density built-up areas, lower wind speeds reduce convective heat exchange at the body's surface. Consequently, even with limited advantages in ambient air temperature, the process of peripheral skin temperature decline is delayed.

The significant increase in SET at noon indicates that solar radiation plays an important physiological compensatory role in extremely cold environments. Heat gained from short-wave radiation can partially offset heat loss due to convection and radiation, while lower wind speeds in high-density built-up areas further slow down peripheral cooling. Unlike WCT, which characterizes instantaneous environmental cold stress, SET directly describes the time required for the human body to reach a specific local cooling threshold. Consequently, it supplements environmental indicators with cumulative physiological information and explains why locations with similar air temperatures but different wind speeds and radiation conditions exhibit varying tolerance durations.



(a) SET (07:00)

(b) SET (12:00)

(c) SET (20:00)

Fig. 5. Spatial distribution of Safe Exposure Time (SET)

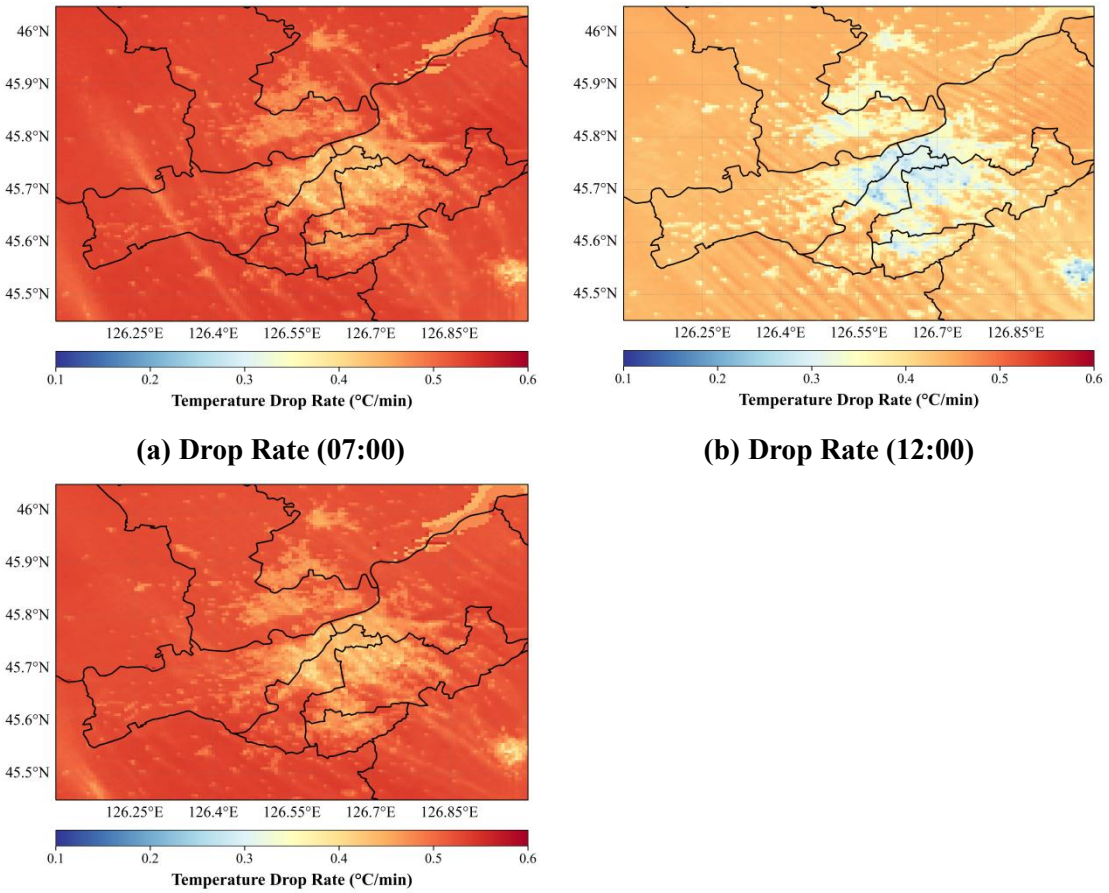
3.3.2 Characteristics of acute cold stress based on skin temperature decline rate

In addition to the duration of tolerance, this study further employed the maximum hand skin cooling rate ($dT_{sk}/dt|_{max,\ i}$) to characterize the intensity of acute cold stress during the initial phase of human exposure. Fig. 6a–c illustrate the spatial distribution of the skin cooling rate across the entire city at three representative time points. The results show that the citywide average skin cooling rate reached 0.518 °C/min and 0.514 °C/min at 07:00 and 20:00, respectively (Table 4), indicating that the human body rapidly undergoes a strong cold stimulus process during the initial phase of exposure. In contrast, the average rate at 12:00 dropped to 0.421 °C/min, and the areas with high cooling rates were significantly reduced, indicating that solar radiation input can effectively slow down the human skin cooling process.

The rate of skin temperature decline in the hands characterizes acute cold stress, which SET alone cannot adequately reflect. Exposure to cold rapidly causes peripheral vasoconstriction, reducing blood flow to the hands and accelerating the local temperature drop; experimental studies have shown that this process is closely associated with an increased sensation of cold and a decline in manual dexterity (Chapman et al., 2025; Lehmuskallio et al., 2002; Orysiak et al., 2024). Therefore, SET and the rate of temperature decline are complementary: the former describes the duration before a threshold is reached, while the latter identifies the areas where cold stimulation is strongest during the initial phase of exposure; together, they characterize the two physiological dimensions of sustained tolerance and acute cooling.

Spatially, urban fringes, riverside areas, and localized ventilation corridors exhibited high rates of temperature decline at all three typical time points, with localized peaks reaching 0.5762°C/min (Table 4). This indicates that, under the conditions of this cold wave, these areas not only have lower ambient temperatures but also expose the human body to rapid cold stimulation more readily during the initial phase of exposure. Combined with SET results, these areas exhibit both a shorter safe exposure time and a higher intensity of acute cold stress, making them physiologically highly sensitive zones that require special attention during this cold snap. In contrast, skin temperature in high-density built-up areas declined relatively

slowly at all three sampling times, demonstrating a stronger physiological buffering effect against cold exposure.



(a) Drop Rate (07:00)

(b) Drop Rate (12:00)

(c) Drop Rate (20:00)

Fig. 6. Spatial distribution of the maximum hand skin cooling rate.

Table 4

Mean values and global statistics of SET and hand skin cooling rate for each LCZ at 07:00, 12:00, and 20:00

	SET (min)			Drop Rate (°C/min)		
	07:00	**12:00**	**20:00**	**07:00**	**12:00**	**20:00**
LCZ1	52.28	113.93	52.99	0.455	0.317	0.452
LCZ2	52.88	119.83	53.20	0.444	0.306	0.443
LCZ3	45.55	116.09	46.37	0.478	0.345	0.473
LCZ4	49.15	115.64	50.04	0.462	0.333	0.458
LCZ5	48.26	116.61	48.77	0.466	0.329	0.463

LCZ6	43.59	111.23	44.55	0.489	0.358	0.483
LCZ7	43.98	111.00	44.82	0.488	0.356	0.484
LCZ8	43.34	107.37	44.28	0.492	0.360	0.487
LCZ9	42.13	102.87	42.78	0.499	0.369	0.495
LCZD	38.86	58.83	39.31	0.526	0.436	0.523
Max	120	120	120	0.576	0.468	0.561
Min	33	49	35	0.351	0.158	0.345
Avg	40.12	67.86	40.61	0.518	0.421	0.514

3.4 Spatiotemporal characteristics of the Cold Exposure Risk Index (CERI)

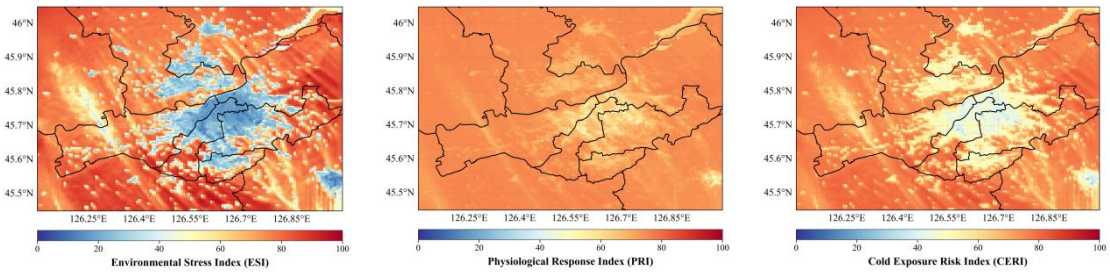
Based on the standardized environmental stress index (ESI) and physiological response index (PRI), a comprehensive cold exposure risk index (CERI) was developed to characterize the coupling between environmental cold stress and human physiological risk during cold waves. Fig. 7 illustrates the spatial distribution characteristics of ESI, PRI, and CERI at 07:00, 12:00, and 20:00.

Table 5 summarizes the mean values and global statistics for ESI, PRI, and CERI in each LCZ at 07:00, 12:00, and 20:00. As shown in Fig. 7 and Table 5, CERI clearly reveals the significant temporal variations and spatial heterogeneity of cold exposure risk in Harbin during the cold wave. At 07:00, the citywide average CERI reached 71.6, with areas classified as higher risk or high risk (CERI > 60) accounting for 84.2% of the total area; by 20:00, the citywide average CERI had dropped to 70.7, and the proportion of higher-risk areas decreased to 78.4%. This indicates that early morning and nighttime are the periods of highest risk of cold exposure; at 12:00, the citywide average CERI dropped to 57.4, with the proportion of high-risk areas (80–100) falling to 0.0%, while the combined proportion of low- and lower-risk areas rose to 16.3%, suggesting that shortwave solar radiation can significantly mitigate the risk of cold exposure.

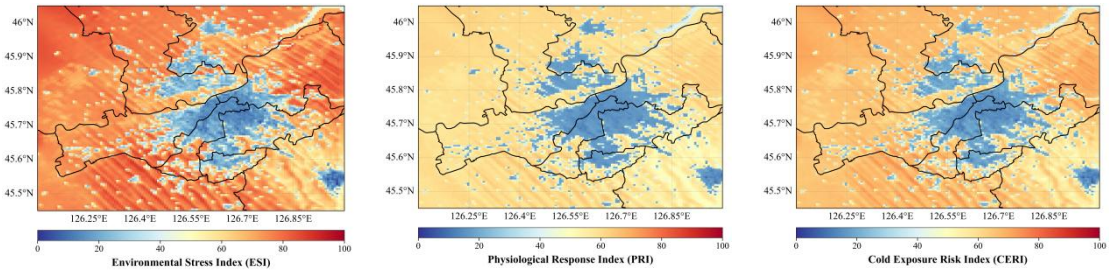
A unified normalization range was applied across the three selected times. Composite-indicator research generally recommends a shared normalization basis for intertemporal comparison, because separately defining extrema at each time changes the

evaluation scale and can obscure actual temporal differences (Becker et al., 2017; Greco et al., 2019). Consequently, identical ESI, PRI, or CERI values have the same relative meaning at 07:00, 12:00, and 20:00, enabling direct comparison of midday risk alleviation and the higher early-morning and nighttime risk.

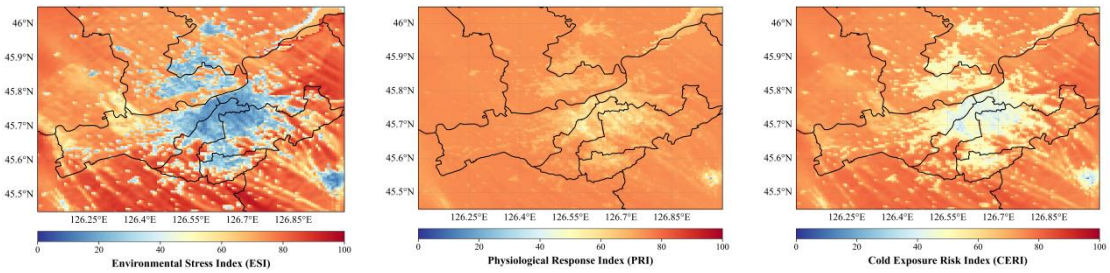
Spatially, the CERI exhibits a distinct “center-to-periphery” increasing distribution pattern. The high-density central urban area maintained a relatively low risk level at all three time points, indicating that its buffering effect against cold exposure exhibits a certain degree of temporal stability. This phenomenon is not solely caused by rising air temperatures, but rather is the combined result of building clusters reducing wind speeds, enhancing long-wave radiation compensation, and reducing convective heat loss from the human body. In contrast, the urban periphery, riverside areas, and outlying farmland and forested areas consistently exhibited continuous high-risk zones, with local CERI peaks reaching 88.4, making them the most sensitive high-risk areas during cold waves. This spatial pattern indicates that the risk of cold exposure in cities during severe cold spells is significantly dependent on topography. High-density built-up areas can create relatively safe microclimatic shelters in winter, whereas open natural surfaces and low-density areas, due to a lack of shelter and thermal storage capacity, are prone to becoming zones where cold exposure risks accumulate over time. Therefore, the CERI results not only reveal the spatial distribution of risks but also further elucidate the mechanism by which urban morphology influences health risks through alterations in human heat exchange processes.



(a1) ESI (07:00) **(b1) PRI (07:00)** **(c1) CERI (07:00)**



(a2) ESI (12:00) **(b2) PRI (12:00)** **(c2) CERI (12:00)**



(a3) ESI (20:00) **(b3) PRI (20:00)** **(c3) CERI (20:00)**

Fig. 7. Spatial distributions of ESI, PRI, and CERI at 07:00, 12:00, and 20:00.

Table 5

Average values and global statistics of ESI, PRI, and CERI for each LCZ at 07:00, 12:00, and 20:00

	ESI			PRI			CERI		
	07:00	**12:00**	**20:00**	**07:00**	**12:00**	**20:00**	**07:00**	**12:00**	**20:00**
LCZ1	27.67	22.56	27.62	63.19	20.07	62.63	48.98	21.07	48.63
LCZ2	18.57	15.83	18.23	62.29	16.02	62.02	44.80	15.94	44.50
LCZ3	29.13	25.02	27.53	68.31	20.25	67.60	52.64	22.16	51.57
LCZ4	29.09	24.64	28.34	65.39	19.87	64.66	50.87	21.78	50.13
LCZ5	27.68	23.04	27.60	66.10	19.10	65.68	50.73	20.67	50.45
LCZ6	33.25	28.91	31.41	70.03	23.77	69.17	55.32	25.83	54.07

LCZ7	32.97	27.31	33.18	69.76	23.78	69.04	55.05	25.19	54.70
LCZ8	39.02	32.83	37.87	70.35	26.09	69.54	57.82	28.78	56.87
LCZ9	40.52	35.39	39.63	71.39	29.22	70.82	59.04	31.69	58.34
LCZD	76.27	72.68	74.69	74.72	58.40	74.28	75.34	64.12	74.44
Max	100.00	90.10	96.71	80.75	65.81	78.77	88.45	75.47	85.58
Min	5.940	1.50	7.43	18.33	8.20	17.97	13.37	4.92	14.06
Avg	68.67	64.9	67.23	73.56	52.32	73.09	71.6	57.35	70.74

3.5 Moderating effect of urban form on physiological cold exposure risk

To further analyze the moderating effect of different urban forms on the risk of human cold exposure, the CERI results were mapped to the LCZ classification system, and the differences in risk levels across different LCZ types were quantified. The box plots in Fig. 8 illustrate the CERI distribution characteristics across LCZs 1–9 and areas with natural land cover. The results indicate significant differences in human cold exposure risk among different urban forms, with an overall trend of gradually increasing risk as building density decreases and spatial openness increases.

Under the selected extreme cold-wave event and standardized human scenario, compact high-density built-up areas (LCZ 1–2) exhibited the most pronounced risk-mitigating effects. Taking LCZ 2 as an example, its average CERI was only 35.08, significantly lower than the domain average. These results indicate that high-density building clusters not only alter the external microclimate but also influence actual cold exposure risk through human heat exchange processes. On the one hand, building clusters increase surface roughness and reduce near-surface wind speeds, thereby decreasing convective heat loss from the human body. On the other hand, dense built environments possess certain heat storage and long-wave radiation compensation effects, which help slow the process of skin temperature decline. Consequently, high-density urban areas can form a relatively stable “physiological buffer zone” during cold waves.

In the LCZ comparison during this cold snap, CERI generally increased as building density decreased and spatial openness increased. CERI in open, low-rise areas (LCZ 6) and

sparsely built-up areas (LCZ 9) was overall higher than in high-density built-up areas. In such areas, insufficient building shelter allows residual wind speeds to exert a stronger influence on convective heat transfer from the human body, accelerating heat loss, shortening the safe exposure time, and intensifying acute cold stress. These results indicate that low-density, sprawling areas may face a higher risk of winter cold exposure under the combined effects of cold waves and strong winds; however, the magnitude of this risk varies depending on wind direction, weather conditions, and specific land-use configurations.

Areas with natural land cover (LCZ D) exhibited the highest risk levels across the study area, with an average CERI of 71.30. Due to the absence of artificial barriers and thermal storage, the combined effects of low temperatures and strong wind chill in open natural areas persistently accumulate, exerting the most severe adverse impact on human thermal balance. Consequently, outlying farmland, forested areas, and riverside zones are the most vulnerable high-risk areas during cold waves. Although these areas may offer cooling and ventilation benefits in summer, they can become sources of cold exposure risk during winter cold waves, illustrating that the climatic effects of urban form exhibit significant seasonal variations.

From a planning perspective, winter climate adaptation design in cities with severe cold should not merely emphasize the continuity of ventilation corridors but should also take into account wind protection at pedestrian height. For waterfront areas, roads along urban peripheries, open squares, and low-density new districts, priority should be given to the provision of windbreaks, semi-enclosed sheltered spaces, composite vegetation barriers, and short-term thermal recovery facilities to reduce the risk of acute cold stress during cold waves. In high-density built-up areas, it is necessary to balance the need for winter wind and cold protection with summer ventilation and heat dissipation requirements, thereby establishing a seasonally adaptive urban climate design strategy.

Overall, urban form can significantly influence cold exposure risk by regulating local wind conditions, thermal radiation, and human heat exchange processes. High-density built-up areas provide a clear buffer against risk in extremely cold environments, whereas low- to medium-density areas and natural open spaces are more prone to forming persistent high-risk cold exposure zones.

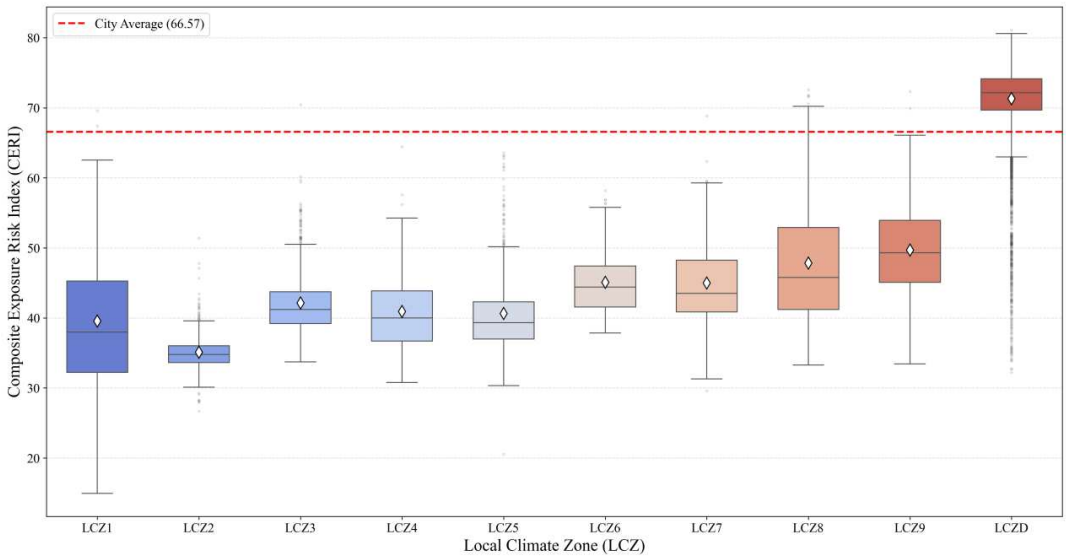


Fig. 8. Distribution of CERI across ordered Local Climate Zones(LCZs)

3.6 Limitations and future work

This study has several limitations. Although the complete winter climate was simulated, the physiological-response and spatial-risk analyses focused on one cold-wave event and three representative times (07:00, 12:00, and 20:00), and therefore do not fully represent cold waves with different intensities, durations, and meteorological conditions. In addition, within the scope of this study, JOS3 simulations used a standardized young male with fixed clothing and activity levels. At this stage, CERI is therefore more appropriate for comparing relative risk among urban forms under a common scenario than for use as an absolute health-risk threshold for the entire population. Future work will extend the framework to multiple cold-wave events and a wider range of population, clothing, and activity scenarios to examine the robustness of urban-form effects and the scalability of CERI.

4 Conclusion

Using the coupled WRF–JOS3 framework, this study established an integrated assessment system linking urban microclimate, human thermophysiological response, and cold exposure risk. A representative cold-wave event in Harbin was used to analyze the spatiotemporal distribution of physiological cold exposure risk and the regulatory role of urban form in a severe-cold city. The main conclusions are as follows:

(1) Urban microclimate showed pronounced spatial heterogeneity during the cold-wave event. In high-density built-up areas (LCZ 1–3), 2 m air temperature was approximately 1.2–1.8 °C

higher and 10 m wind speed was approximately 71%–74% lower than in peripheral areas. Compared with the air-temperature difference, urban-form-induced variation in pedestrian-level wind was an important contributor to spatial differences in cold exposure in this case.

(2) Urban form substantially influenced thermophysiological response under the standardized human, clothing, and activity scenario. In high-density built-up areas, WCT was approximately 7.3–7.5 °C higher than in open areas, mean SET was extended by 4–6 min, and the hand skin cooling rate decreased by approximately 0.08 °C/min. These results indicate that wind shelter reduced convective heat loss and delayed peripheral cooling during the selected event.

(3) Physiological cold exposure risk differed among the three selected times. Mean CERI values were 71.6 at 07:00 and 70.7 at 20:00, compared with 57.4 at 12:00 when solar-radiation input was stronger. Peripheral open areas, waterfronts, and low-density areas showed relatively high risk during the event, whereas high-density built-up areas exhibited a relative risk-buffering effect.

(4) CERI extends the assessment of external environmental cold stress toward dynamic physiological response. WCT represents atmospheric cold hazard, whereas SET and hand skin cooling rate represent the response rate and intensity produced after environmental conditions are modified by clothing, radiative heat exchange, and human thermoregulation. Their integration provides information on tolerance time and acute peripheral cooling that air temperature or WCT alone cannot express. CERI is therefore suitable for comparing relative physiological cold exposure risk among urban forms under a common scenario and can support human-scale cold-wave adaptation strategies.

Declarations

Author contributions

Y.X.: Conceptualization, methodology, software, formal analysis, data curation, visualization, and writing—original draft. X.C.: Methodology, validation, data curation, and writing—review and editing. J.C.: Conceptualization, supervision, project administration, funding acquisition, and writing—review and editing. L.L.: Formal analysis, visualization, and

writing—review and editing. B.W.: Formal analysis, visualization, and writing—review and editing. All authors reviewed and approved the final manuscript.

Data availability

The data generated and analyzed during the current study are available from the corresponding author upon reasonable request.

Competing interests

The authors declare that they have no competing interests.

Funding

This work was supported by the Heilongjiang Provincial Natural Science Foundation of China (Grant No. PL2024E009), and the National Natural Science Foundation of China (Grant No. 52108072).

References

Allen-Dumas, M. R., Sweet-Breu, L. T., Brelsford, C. M., Wang, L., New, J. R., & Bass, B. C. (2024). Sensitivity of mesoscale modeling to urban morphological feature inputs and implications for characterizing urban sustainability. *npj Urban Sustainability*, *4*(1), 49. https://doi.org/10.1038/s42949-024-00185-6

Arias, P., Bellouin, N., Coppola, E., Jones, R., Krinner, G., Marotzke, J., Naik, V., Palmer, M., Plattner, G.-K., & Rogelj, J. (2021). Climate Change 2021: the physical science basis. Contribution of Working Group I to the Sixth Assessment Report of the Intergovernmental Panel on Climate Change; technical summary. https://doi.org/10.1017/9781009157896.002

Assaad, D. A., Rupp, R. F., Toftum, J., Breesch, H., & van Hooff, T. (2025). Multi-segmentation of JOS-3 thermoregulation model: Validation under steady-state and transient conditions. *Building and Environment*, *270*, 112560. https://doi.org/10.1016/j.buildenv.2025.112560

Becker, W., Saisana, M., Paruolo, P., & Vandecasteele, I. (2017). Weights and importance in composite indicators: Closing the gap. *Ecological Indicators*, *80*, 12-22. https://doi.org/10.1016/j.ecolind.2017.03.056

712 Bu, Y., Sun, Z., Tao, Y., Ruan, W., Zhang, X., Liang, Y., & Zhao, Y. (2025). Assessing cold
713 exposure risk during cold waves in Beijing using high spatiotemporal resolution
714 population data and temperature variations. *Environment International*, *203*, 109773.
715 https://doi.org/10.1016/j.envint.2025.109773
716 Cao, J., Cao, S., Ma, Z., & Liu, L. (2023). Diffusion characteristic of air pollutant from
717 district heating source driven by urban wind field and layout optimization. *Journal of*
718 *Wind Engineering and Industrial Aerodynamics*, *239*, 105462.
719 https://doi.org/10.1016/j.jweia.2023.105462
720 Cao, J., Mao, R., Ning, H., & Shui, T. (2024). Exploring the natural ventilation potential for
721 supertall buildings considering vertical meteorology: A case study in Harbin, China.
722 *Applied Thermal Engineering*, *239*, 122163.
723 https://doi.org/10.1016/j.applthermaleng.2023.122163
724 Chapman, C. L., Roberts, B. M., Schafer, E. A., Castellani, J. W., Friedl, K. E., Potter, A. W.,
725 & Looney, D. P. (2025). Occupational cold stress and rewarming alters skin
726 temperature thresholds for manual dexterity decrements: An exploratory study.
727 *Physiological Reports*, *13*(9), e70342. https://doi.org/10.14814/phy2.70342
728 Choudhary, B., & Udayraj. (2023). Validity of the JOS-3 model for male tropical population
729 and analysis of their thermal comfort. *Sādhanā*, *48*(4), 208.
730 https://doi.org/10.1007/s12046-023-02254-5
731 Dharmasastha, K., Liang, H., Lin, J., Xie, Y., Yu, Y., & Niu, J.-l. (2024). Evaluating thermal
732 sensation in outdoor environments-Different methods of coupling CFD and radiation
733 modelling with a human body thermoregulation model. *Building and Environment*,
734 *266*, 112081. https://doi.org/10.1016/j.buildenv.2024.112081
735 Di Napoli, C., Hogan, R. J., & Pappenberger, F. (2020). Mean radiant temperature from
736 global-scale numerical weather prediction models. *International Journal of*
737 *Biometeorology*, *64*(7), 1233-1245. https://doi.org/10.1007/s00484-020-01900-5
738 Gál, T., Alinasab, N., Abdulhaq, H. A., & Skarbit, N. (2025). A Structured Literature Review
739 of the Application of Local Climate Zones (LCZ) in Urban Climate Modelling. *Earth*,
740 *7*(1), 3. https://doi.org/10.3390/earth7010003

Georgescu, M., Broadbent, A. M., & Krayenhoff, E. S. (2024). Quantifying the decrease in heat exposure through adaptation and mitigation in twenty-first-century US cities. *Nature Cities*, *1*(1), 42-50. https://doi.org/10.1038/s44284-023-00001-9

Greco, S., Ishizaka, A., Tasiou, M., & Torrisi, G. (2019). On the Methodological Framework of Composite Indices: A Review of the Issues of Weighting, Aggregation, and Robustness. *Social Indicators Research*, *141*(1), 61-94. https://doi.org/10.1007/s11205-017-1832-9

Hanna, S. R., & Yang, R. (2001). Evaluations of Mesoscale Models' Simulations of Near-Surface Winds, Temperature Gradients, and Mixing Depths. *Journal of Applied Meteorology*, *40*(6), 1095-1104. https://doi.org/10.1175/1520-0450(2001)040<1095:EOMMSO>2.0.CO;2

He, X., Li, Y., Wang, X., Chen, L., Yu, B., Zhang, Y., & Miao, S. (2019). High-resolution dataset of urban canopy parameters for Beijing and its application to the integrated WRF/Urban modelling system. *Journal of Cleaner Production*, *208*, 373-383. https://doi.org/10.1016/j.jclepro.2018.10.086

Huang, J., Huang, Z., & Liu, W. (2025). Combining the WRF model and LCZ scheme to assess spatiotemporal variations of thermal comfort in Shenzhen's built-up areas. *Sustainable Cities and Society*, *122*, 106252. https://doi.org/10.1016/j.scs.2025.106252

Huang, X., Chang, J. M.-H., Shi, D., Chan, P. W., & Song, J. (2025). WRF-HEATS coupling: Incorporating human behaviors and city topography into urban heat stress evaluation. *Building and Environment*, *267*, 112191. https://doi.org/10.1016/j.buildenv.2024.112191

Joshi, A., Twidwell, B., Park, M., & Rykaczewski, K. (2025). Comparative analysis of thermoregulation models to assess heat strain in moderate to extreme heat. *Journal of Thermal Biology*, *127*, 104035. https://doi.org/10.1016/j.jtherbio.2024.104035

Kacker, K., Srivastava, P., & Mukherjee, M. (2024). Heat stress risk at an intra-urban level: A case study of Delhi, India. *Building and Environment*, *264*, 111897. https://doi.org/10.1016/j.buildenv.2024.111897

Kong, S., Liu, L., & Cao, J. (2025). Developing local-climate-zone-based logarithmic law wind profile considering urban morphology. *Urban Climate*, *59*, 102246. https://doi.org/10.1016/j.uclim.2024.102246

Kong, S., Xiao, Y., Cao, J., & Han, Z. (2025). Adapting wind shear coefficients to urban morphology: Unlocking urban wind energy potential. *Sustainable Cities and Society*, *121*, 106217. https://doi.org/10.1016/j.scs.2025.106217

Lehmuskallio, E., Hassi, J., & Kettunen, P. (2002). The skin in the cold. *International journal of circumpolar health*, *61*(3), 277-286. https://doi.org/10.3402/ijch.v61i3.17475

Liang, H., Tanabe, S. I., & Niu, J. (2023). Coupled simulation of CFD and human thermoregulation model in outdoor wind environment. E3S Web of conferences,

Lin, J., Jiang, Y., Xie, Y., & Niu, J. (2025). A novel method for local clothing insulation prediction to support sustainable building and urban design. *International Journal of Biometeorology*, *69*(8), 1899-1917. https://doi.org/10.1007/s00484-025-02934-3

Lin, L., Luo, M., Chan, T. O., Ge, E., Liu, X., Zhao, Y., & Liao, W. (2019). Effects of urbanization on winter wind chill conditions over China. *Science of the Total Environment*, *688*, 389-397. https://doi.org/10.1016/j.scitotenv.2019.06.145

Lv, L.-S., Yin, L., Liu, Y., Zhou, C.-L., Hu, J., An, N., Xie, X., Zhang, X.-E., Zhang, M., & Liu, X.-Y. (2025). The effect of heatwave and cold spell on cardiovascular disease mortality in central China, 2018–2022. *International Journal of Biometeorology*, *69*(3), 581-589. https://doi.org/10.1007/s00484-024-02836-w

Martilli, A., Nazarian, N., Krayenhoff, E. S., Lachapelle, J., Lu, J., Rivas, E., Rodriguez-Sanchez, A., Sanchez, B., & Santiago, J. L. (2024). WRF-Comfort: simulating microscale variability in outdoor heat stress at the city scale with a mesoscale model. *Geoscientific Model Development*, *17*(12), 5023-5039. https://doi.org/10.5194/gmd-17-5023-2024

Nie, Y., Sun, Y., Zhang, X., & Chen, G. (2025). Human-induced changes in extreme cold surges across the Northern Hemisphere. *Nature Communications*, *16*(1), 8086. https://doi.org/10.1038/s41467-025-62576-2

Orysiak, J., Młynarczyk, M., & Irzmańska, E. (2024). The effect of exposure to cold on dexterity and temperature of the skin and hands. *International Journal of*

Occupational Safety and Ergonomics, *30*(1), 64-71. https://doi.org/10.1080/10803548.2023.2293387

PoshtMashhadi, A., Maghsoodi, A. I., & Wood, L. C. (2025). The impact of extreme temperatures on emergency department visits: A systematic review of heatwaves, cold waves, and daily temperature variations. *Science of the Total Environment*, *970*, 178869. https://doi.org/10.1016/j.scitotenv.2025.178869

Saaty, T. L. (1980). The analytic hierarchy process. ISBN：0070543712

Schmidt, K., Aumann, I., Hollander, I., Damm, K., & von der Schulenburg, J. M. (2015). Applying the Analytic Hierarchy Process in healthcare research: A systematic literature review and evaluation of reporting. *BMC Med Inform Decis Mak*, *15*, 112. https://doi.org/10.1186/s12911-015-0234-7

Schober, P., Boer, C., & Schwarte, L. A. (2018). Correlation Coefficients: Appropriate Use and Interpretation. *Anesthesia & Analgesia*, *126*(5), 1763-1768. https://doi.org/10.1213/ANE.0000000000002864

Smithson, C., & Adams, B. R. (2024). Use of LCZs with urban canopy modeling to evaluate urban growth effects on meteorological conditions in the Salt Lake Valley. *Urban Climate*, *57*, 102106. https://doi.org/10.1016/j.uclim.2024.102106

Takahashi, Y., Nomoto, A., Yoda, S., Hisayama, R., Ogata, M., Ozeki, Y., & Tanabe, S.-i. (2021). Thermoregulation model JOS-3 with new open source code. *Energy and Buildings*, *231*, 110575. https://doi.org/10.1016/j.enbuild.2020.110575

Vellei, M., de Dear, R., Le Dreau, J., Nicolle, J., Rendu, M., Abadie, M., Michaux, G., & Doya, M. (2022). Dynamic thermal perception under whole-body cyclical conditions: Thermal overshoot and thermal habituation. *Building and Environment*, *226*, 109677. https://doi.org/10.1016/j.buildenv.2022.109677

Wang, F., Xu, H., Lei, T.-H., Xu, Y., Wang, H., & Wang, L. (2025). Defining human thermoregulation limits: a critical evaluation of predictive models using healthy young adults. *American Journal of Physiology-Regulatory, Integrative and Comparative Physiology*, *329*(4), R524-R533. https://doi.org/10.1152/ajpregu.00108.2025

Wang, L., Liu, J., Yin, P., Gao, Y., Jiang, Y., Kan, H., Zhou, M., Ao, H., & Chen, R. (2024). Mortality risk and burden of sudden cardiac arrest associated with hot nights, heatwaves, cold spells, and non-optimum temperatures in 0.88 million patients: an individual-level case-crossover study. *Science of the Total Environment*, *949*, 175208. https://doi.org/10.1016/j.scitotenv.2024.175208

Wei, L., & Sobrino, J. A. (2025). Heat resilience assessment during a heatwave based on WRF-simulated UTCI: Insights from built LCZ types in Valencia, Spain. *Urban Climate*, *64*, 102672. https://doi.org/10.1016/j.uclim.2025.102672

Xu, X., Rioux, T. P., & Castellani, M. P. (2023). Three dimensional models of human thermoregulation: A review. *Journal of Thermal Biology*, *112*, 103491. https://doi.org/10.1016/j.jtherbio.2023.103491

Zhao, J., Wang, Y., Ou, D., Wang, H., Li, Y., & Deng, Q. (2024). Predicting survival time for cold exposure by thermoregulation modeling. *Building and Environment*, *249*, 111127. https://doi.org/10.1016/j.buildenv.2023.111127

Zhao, Q., Guo, Y., Ye, T., Gasparrini, A., Tong, S., Overcenco, A., Urban, A., Schneider, A., Entezari, A., & Vicedo-Cabrera, A. M. (2021). Global, regional, and national burden of mortality associated with non-optimal ambient temperatures from 2000 to 2019: a three-stage modelling study. *The Lancet Planetary Health*, *5*(7), e415-e425. https://doi.org/10.1016/S2542-5196(21)00081-4